POLITECNICO
MILANO 1863

SCUOLA DI INGEGNERIA INDUSTRIALE
E DELL'INFORMAZIONE

Executive Summary of the Thesis

Galactic Cosmic Rays Characterization with ESA Planetary Missions

Laurea Magistrale in Mathematical Engineering - Ingegneria Matematica

Author: Thomas Rimbot

Advisor: Prof. Luca Formaggia

Academic year: 2022-2023

1. Introduction

Space exploration is one of the major current and future challenges of humanity, in particular because of the harsh conditions of the space environment, for instance radiation. On Earth, the atmosphere absorbs or reflects most of the radiation that is deadly to humans, allowing life to thrive. In space and to varying degrees on other planets, no such natural protection is present. Thus, careful understanding of the space radiation environment is necessary to design appropriate counter-measures for astronauts and spacecrafts. At the high-end of the radiation energy spectrum are particles coming from *Galactic Cosmic Rays* (GCRs). Because of their high energy, they are particularly hazardous to electronics systems and humans, thus motivating the need to accurately characterize them.

In order to characterize galactic cosmic rays and the space radiation environment in general, some spacecrafts carry *radiation monitors*. These instruments are built to detect high energy charged particles with specialized detectors. Processing the resulting data allows to understand the environment around the spacecraft. As the mission JUICE has just been launched on April 14th 2023, its radiation monitor, the *RADiation-hard Electron Monitor* (RADEM) [5], should be accurately characterized for future studies. One of its four detectors, the *Heavy-Ion Detector Head* (HIDH), was not studied yet. The main goal of this project was to run simulations of particle interactions with the HIDH and analyse the resulting data to characterize the detector's properties. This implied simulating GCRs fluxes to identify their most abundant elements, developing a first order computation framework to better understand the underlying processes of particles-detector interactions, and running advanced simulations with a dedicated software (`Geant4`) to characterize the detector's properties in multiple settings.

Another focus of this work was the use of engineering parameters in GCRs characterization at Venus. These parameters are the *Error Detection And Correction* (EDAC) cumulative counters, used for detection and correction of errors induced by highly energetic charged particles hitting a spacecraft's memory devices. The relationship between high-energy GCRs particles and the EDAC was developed in [3] and reproduced here on *Venus Express* data. As long duration radiation data at Venus is not available to this day, this work represents one of the first characterization of galactic cosmic rays so close to the Sun over a long period of time.

2. Theoretical framework

This section introduces the fundamentals of particles-detector interactions.

2.1. Elements of particles-space detector interactions

RADEM contains detector heads referred to as *Stack Detectors*. Each head is an arrangement of layers through which the particles pass one after the other. As the particle goes through the layers, it loses energy by coloumbic deposition. Layers can purely slow down the particle (absorbers) or measure the deposited energy (diodes). The more energetic the particle is, the deeper it goes in the detector. Mathematically, the deposited energy E_d of a particle with primary energy E_0 can be found from the stopping power P of the medium, its density ρ, and the range l travelled by the particle:

$$E_d = \max(E_0, P \cdot \rho \cdot l). \quad (1)$$

If the particle deposited all of its energy into the layer, it embedds itself into the medium. .

2.2. Radiation monitoring on JUICE

RADEM is a radiation monitor developed for analyzing energetic particles present in the harsh radiation environment around Jupiter. It allows to set lower thresholds on the minimal deposited energy of a particle on the HIDH diodes. These are charge values $C_0 \in [C_{\min}, C_{\max}]$ such that only particles inducing at least $C \geq C_0$ fC on the diode are considered. It contains four detector heads. The *Heavy-Ion Detector Head* (*HIDH*) is designed for ions found in GCRs. It allows discrimination of heavy ions (atomic number $z \geq 2$) up to Oxygen ($z = 8$). It is composed of an arrangement of 300μm-thick Silicon diodes, with Aluminium and Tantalum absorbers.

2.3. Detector properties

Several properties are of interest to characterize the detector.

2.3.1 Field of view

The *Field of View* (FOV) of a detector is defined as the solid angle through which it is sensitive to incoming particles. From Figure 1, the HIDH's FOV is $\eta = 45°$.

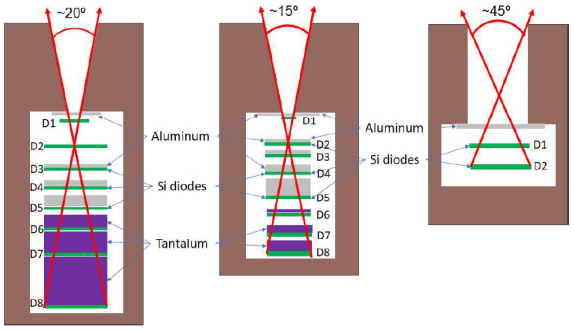

Figure 1: Schematics of the PDH (left), EDH (center) and HIDH (right). From [5].

2.3.2 Geometric factor

The response functions of the detector's diodes are defined in terms of their *Geometric Factor* as a function of the primary energy of the incident particles. It represents the probability that a particle with given energy E can interact with the diode. Under assumptions described in [6], the ideal geometric factor G_i of each diode $i \in \{1, 2\}$ can be computed from its radius R_i and depth l_i as:

$$G_i = \frac{1}{2}\pi^2[R_0^2 + R_i^2 + l_i^2 - \sqrt{(R_0^2 + R_i^2 + l_i^2)^2 - 4R_0^2R_i^2}]. \quad (2)$$

In practice, the effective geometric factor is different from this theoretical value, as it depends on the particles' primary energy, their distribution and their interactions with the diodes. The effective geometric factor $\tilde{G}_i(E)$ of a diode for particles with primary energy E is found as a weighted ratio between the number of particles with primary energy E interacting with diode i and the total number of source particles with this energy:

$$\tilde{G}_i(E) = A\pi\frac{N_i(E)}{N(E)}. \quad (3)$$

2.3.3 Count rates

Another interesting property of the detector is the diodes' *Count Rates*, *i.e.* the number of counts a diode registers each second, in s^{-1}. It is inferred from the local particle flux $\phi(E)$ and the geometric factor via:

$$R_i = \int_0^\infty \phi(E)G_i(E)\mathrm{d}E. \quad (4)$$

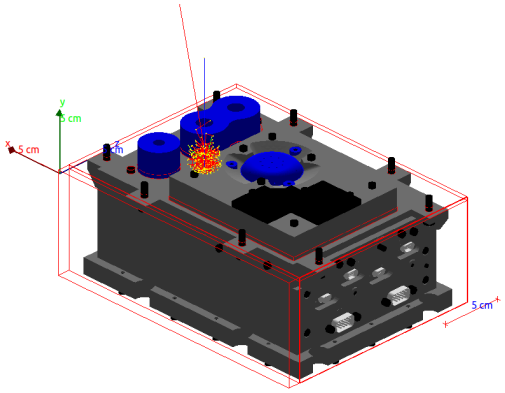

Figure 2: `Geant4` simulation output for a straight beam of Oxygen particles on the HIDH.

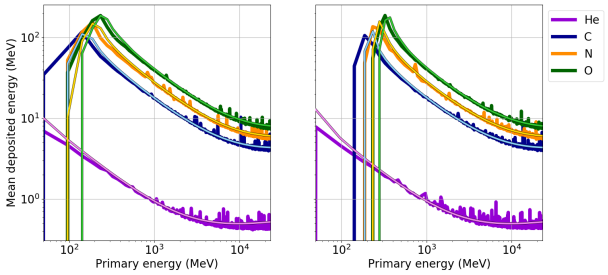

Figure 3: Simulations with `Geant4` (simple solid lines) and `FOCom-PDI` (lighter lines with black outlines) between a straight beam of GCRs particles and the HIDH diodes 1 (left) and 2 (right).

3. Numerical simulations of the RADEM response to GCRs particle fluxes

This section describes how the RADEM simulations were run and used to characterize the detector's properties.

3.1. GCRs flux analysis with PyCREME

Using `PyCREME`, a GCRs flux was simulated for a given date and used to understand the most abundant elements in GCRs: Helium ($z = 2$), Carbon ($z = 6$), Nitrogen ($z = 7$) and Oxygen ($z = 8$) with main energy range in $[10^1, 10^3]$ MeV/AMU. These were then simulated through the detector with energy range $[0.05, 23]$ GeV. Since most particles are expected to be on the lower end of the energy spectrum, an Inverse Power Law was used for the energy distribution. This was also useful for practical reasons, as lower energy particles are stopped more easily in the material, which reduced the computation time.

3.2. Point source simulation

The first source shape is a point source, resulting in a straight beam of particles shooting right in the middle of the HIDH. The `Geant4` setting is shown in Figure 2, where the vertical blue line represents the incoming beam of particles which interact with the different layers and scatter (red lines), depositing energy in the process.

A first order framework was also developed in `Python3` to get an initial estimate on the physical processes behind these interactions. It was named `FOCom-PDI` for *First-Order Computation for Particle-Detector Interactions*. For each type of particle, the primary energy range $[0.05, 23]$ GeV was simulated with a uniform discrete grid of 500 points. The software performs the computation for the passage of the particle through each layer and keeps track of the deposited energy measured by the two diodes. The results were compared to `Geant4`, which is based on Monte-Carlo simulations.

Figure 3 reports the results of these simulations for GCRs particles. The mean deposited energy is consistently higher for heavier elements. This is because these elements tend to interact more with the medium and hence deposit more energy. However, the profiles for all particles follow the same exponential decrease. As a particle's primary energy increases, its speed increases as well and it interacts less with the medium, depositing less energy. Despite a few noticeable differences, the first order computation scheme yields similar results to the Monte Carlo-simulations.

3.3. Plane source and characterization of the HIDH response

Particles in space do not collide with the detector in a straight beam in the center of the head but are omni-directional. Consequently, simulations with a more realistic plane source setting assuming an omni-directional flux were performed. From these, detector characteristics like its field of view and count rates were then computed. Figure 4 displays a graphical representation of the plane source setting with a focus on the HIDH. Particles originate from

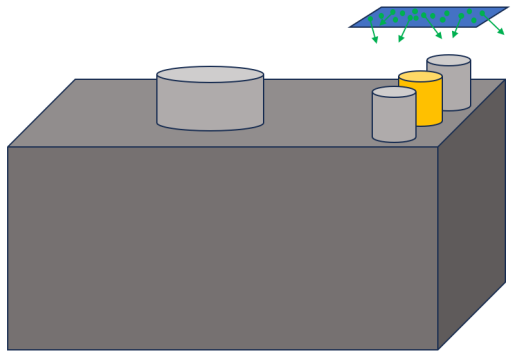

(a) Wide view.

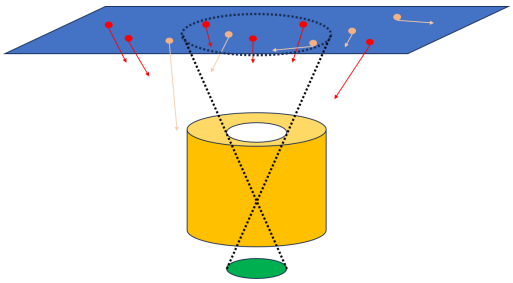

(b) Focus on the HIDH.

Figure 4: Graphical representation of the plane source setting.

the plane with various directions and energies. Those within the field of view and with an angle less than half of it will almost always penetrate the aperture and interact with the diodes if they pass the absorber. Those outside the field of view can only interact with the diodes if their energy is high enough to make them penetrate the collimator.

3.3.1 Field of view

The validation of the FOV from the simulation results is reported in Figure 5, where the incidence angle of Carbon, Nitrogen and Oygen particles interacting with diodes 1 and 2 is shaped like a normal distribution in the range $[0°, 22.5°]$. Helium particles reach higher values, with a distribution in the range $[0°, 40°]$. This is due to the fact that lighter particles like Helium interact less with the medium with respect to heavier particles. They deposit less energy and are hence able to travel greater distances through dense mediums. Thus, even with a reduced energy range, Helium particles outside the field of view are still able to penetrate the collimator and reach the diodes by going through it.

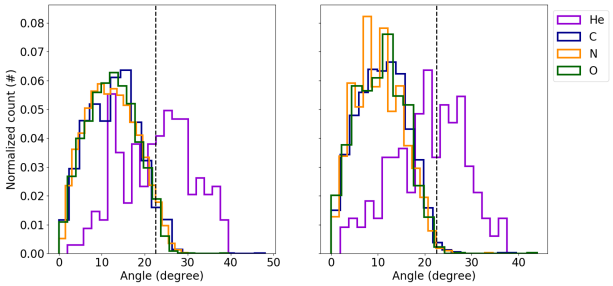

Figure 5: Normalized distribution of the primary angle of source particles hitting diodes 1 (left) and 2 (right).

The particles' position on the starting plane source yields informative results as well. Displaying these positions on a grid allows to determine the spatial distribution of interacting particles. As can be seen on Figure 6, the position of source particles hitting the diodes indeed forms a two-dimensional Gaussian distribution centered on the aperture (green circle). Particles outside the aperture can be nonetheless within the field of view and still hit the diodes. Finally, high-energy particles can go through the collimator (black circle) and register a hit even though they are far from the center. This is especially visible on the top subplots corresponding to the lighter Helium particles. Since light elements interact less with the medium, they can travel further inside and reach the diodes from the side. This correlates to the higher values of the angle for Helium particles found in Figure 5. Note that this effect decreases as the atomic number increases.

3.3.2 Geometric factor

The effective values of the geometric factors as a function of the particles' primary energy were computed from Equation 3. Figure 7 displays the theoretical and computed geometric factors of the two HIDH diodes for the main GCRs particles. Since the geometric factors depend on the effective threshold of the diodes, different plots are obtained depending on the chosen combination. Figure 7a reports the results for no threshold ($t_1 = 0$ DAC, $t_2 = 0$ DAC) and Figure 7b the current setting on the HIDH ($t_1 = 52$ DAC, $t_2 = 244$ DAC). The black dashed lines represent the theoretical values computed from Equation 2.

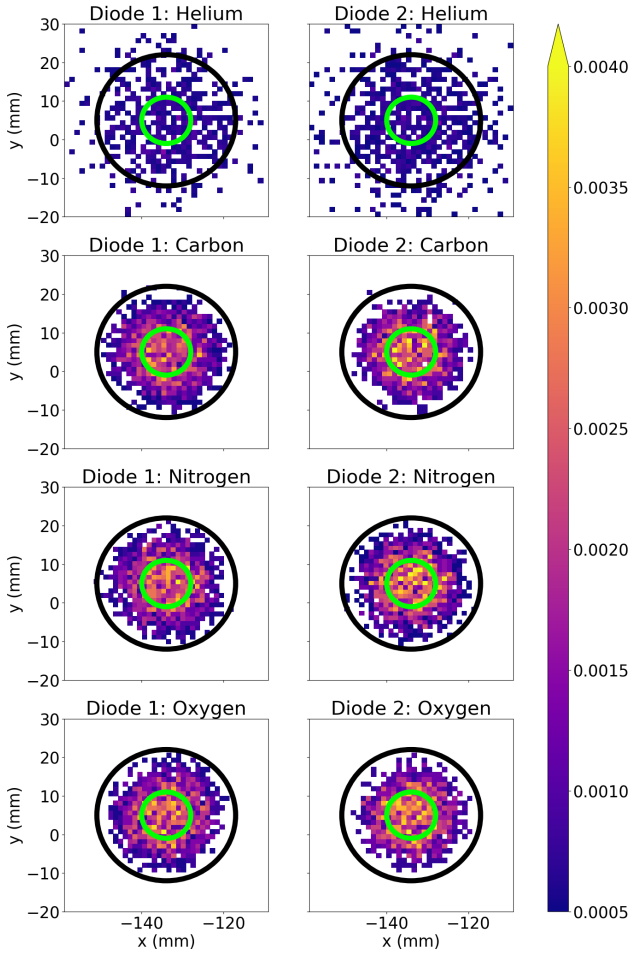

Figure 6: Normalized density distribution of the primary position of source particles hitting diodes 1 and 2.

The computations with no thresholds yield a curve with a step function-like shape for low energies, corresponding to the minimum required energy to reach the diodes. The effective geometric factors match the theoretical values for low energy particles. For higher energies, the computed geometric factors increase above this value. This is because highly energetic particles can penetrate the collimator and still interact with the diodes, even if they do not go through the aperture. On the other hand, the non-zero thresholds combination plots exhibit a square-like shape with a first spike to a constant value, later followed by a drop and a lower valued tail. The drop represents the trend of the stopping power for highly energetic particles: as these go faster and interact less with the matter, they deposit less energy. Therefore, particles with energy above a certain value will not deposit as much energy as the low energy ones and trigger less response in the diodes, leading to a smaller geometric factor.

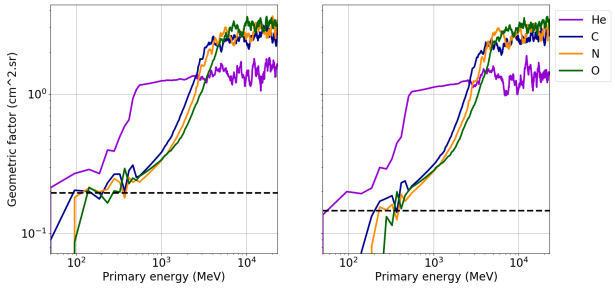

(a) No thresholds on the diodes: $t_1 = 0$ DAC, $t_2 = 0$ DAC.

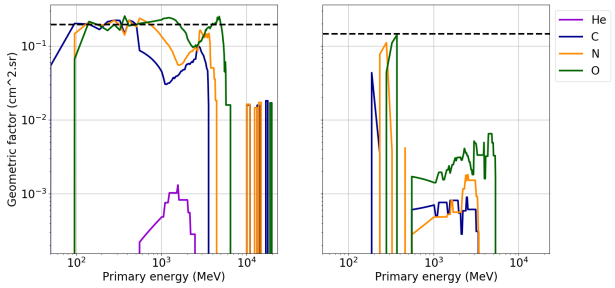

(b) Current thresholds on the diodes: $t_1 = 52$ DAC, $t_2 = 244$ DAC.

Figure 7: Geometric factors computed from the plane simulations.

3.4. Count rates

In practice, the instrument does not give access to the geometric factors, as these are purely theoretical properties. Instead, it outputs counts, *i.e.* the number of particles registering a hit on each diode.

3.4.1 Influence of the lower thresholds

The count rates were first computed with thresholds varying in the range $[C_{\min}, C_{\max}]$. This allowed to describe each diode's count rates as a function of its lower threshold. The results are displayed in Figure 8 for the two HIDH diodes. As expected, increasing the thresholds induces a decrease in the count rates, until a threshold too high is reached and no count is registered. The count rates corresponding to lighter elements drop faster than for heavier elements because lighter elements deposit less energy.

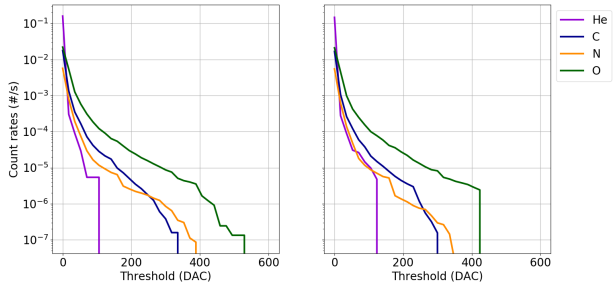

Figure 8: Count rates computed from the plane simulations as a function of the diodes' lower thresholds. The subplots correspond to the HIDH diodes 1 (left) and 2 (right).

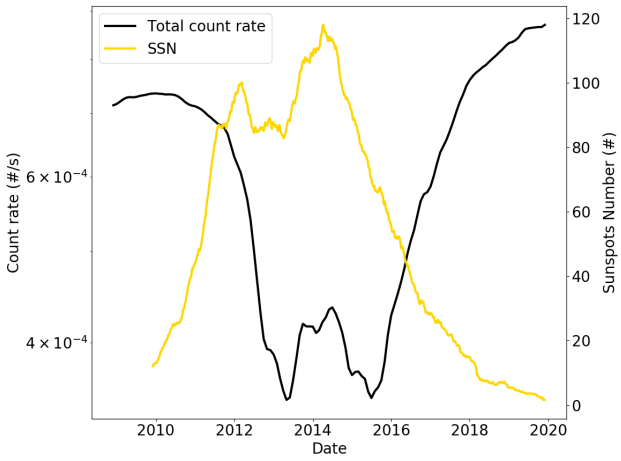

Figure 9: Total count rates on the HIDH first diode (black curve) and Sunspots Number (yellow curve) during the solar cycle 24.

3.4.2 Solar temporal modulation

The solar cycle exerts a temporal modulation on the GCRs intensity via an anti-correlation relationship. As the count rates of the detector are obtained by convolving the flux with the geometric factors, this modulation should also be visible in the count rates values computed over a longer period of time. To this end, the GCRs flux was simulated for the whole solar cycle 24. The count rates were then computed using the same methods as in the previous subsections. The total count rate of the detector was computed and is displayed in Figure 9 together with the solar activity using the Sunspots Number (yellow curve) during this same period.

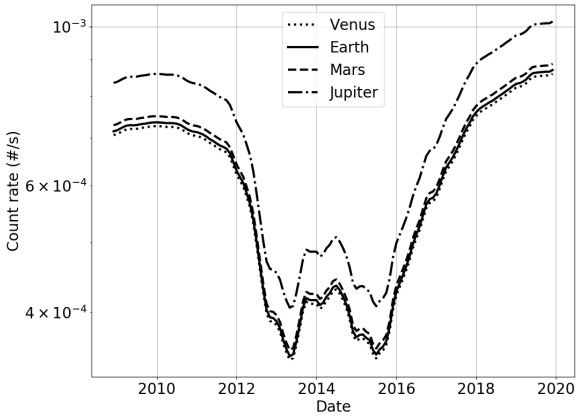

Figure 10: Total count rates on the HIDH first diode computed from a simulated GCRs flux at different planets during the solar cycle 24.

The expected anti-correlation is clearly visible. The minimum value of the count rates is about 60% lower than the maximum value. The anti-correlation is also shifted as the count rates variation lags behind the solar activity's. It lags behind by about 11 months, which is close to the results reported in the literature for the GCRs time-lag at Earth [1, 3].

3.4.3 Solar spatial modulation

The GCRs intensity is also known to exhibit a spatial variation of about $4\%.\mathrm{A\,U}^{-1}$ with heliocentric distance. In mathematical terms, let g_1 and g_2 be the GCRs intensity in two points aligned with the Sun, d_1 and d_2 their heliocentric distance and $\gamma = 0.04$. Then:

$$g_2 = g_1(1 + \gamma(d_2 - d_1)). \tag{5}$$

To assess the influence of this modulation on the count rates, a GCRs flux was simulated for 3 additional planets: Venus (0.7 A U), Mars (1.5 A U) and Jupiter (5.2 A U). The resulting count rates curves are displayed in Figure 10.

The results are as expected: the curves are ordered according to the heliocentric distances and computing the ratio between these count rates and the Earth count rates yields the aforementioned factor. This analysis therefore shows how the spatial modulation of GCRs fluxes can be captured from the output of the radiation monitor.

3.5. Discussion

After understanding the most abundant elements in GCRs fluxes, simulations were run for a point source with a first order framework (`FOCom-PDI`) and a dedicated particle-through-matter simulation software (`Geant4`). `FOCom-PDI` resulted very satisfying for this simple setup. A more realistic plane source was afterwards used with `Geant4` to capture some of the detector's properties. Its field of view and geometric factors were computed from the simulation results and compared to the theoretical values. In general, these match pretty well but they depend on several factors, the two main ones being the thresholds configuration and the energy of the particles. It was also shown that particles with higher energies can penetrate the collimator and interact with the diodes, directly impacting the field of view and geometric factor computations. This can be mitigated using different thresholds configurations on the HIDH, as these particles tend to deposit less energy on the diodes. Finally, the diodes' count rates were computed by convolving the geometric factors with the particles fluxes.

The temporal modulation of the solar activity was investigated by generating a GCRs flux over the solar cycle 24. This temporal variation appears to have a greater impact on the count rates than on the GCRs flux (30% to 60% against the 20% theoretical value). The spatial modulation was studied as well by manually generating a GCRs flux at Venus, Mars and Jupiter based on the radial gradient $\gamma = 4\%\mathrm{A\,U}^{-1}$ and was straightforwardly derived from the count rates profiles.

Several uncertainties stem from the simulations. First of all, the limited energy range $[0.05, 23]$ GeV reduces the accuracy of the results, as high energy particles are known to have a significant impact on the detector's readings. However, this choice was justified by conducting a quantitative analysis on the stabilization of the computed properties. This range was estimated sufficient to get a very good estimate on these. The number of particles used in the simulations is a source of error as well, since too few particles in the random Monte-Carlo process would not allow to draw confident conclusions from the reported findings. This was assessed and shown to be acceptable for the cases of interest. Some ways of increasing the statistics include combining the two diodes and computing the counts over a longer period of time. Increasing the number of simulated particles could improve the results but comes with longer computation times which were not achievable in the timeframe of this thesis.

The main goal of this project was attained. Nonetheless, it would be interesting to run longer and denser simulations in order to improve on these results. These findings should also be compared against real JUICE data when available, especially in 2032 when it has reached the Jovian system.

4. Using EDAC counters for GCRs characterization with *Venus Express* data

A spacecraft carries several memory devices that are constantly hit by energetic particles. When an energetic particle hits the spacecraft, *Single Event Upsets* (SEUs) [4] can occur, triggering bit flips in the memory and effectively corrupting it. These events are non-destructive and can thus be detected and corrected on board the spacecraft with an *Error Detection And Correction* (EDAC) algorithm [2]. After the correction is done, the corresponding EDAC counter is incremented by 1 unit. There is a relatively steady cumulative EDAC increase, attributed to the continuous presence of cosmic rays since only high energetic particles are expected to trigger an SEU. The counter can also exhibit sporadic sudden increases due to *Solar Energetic Particles* (SEPs) events, during which the Sun emits a lot of these highly energetic particles which can hit the spacecraft and induce SEUs.

The EDAC counter, as engineering data, is in principle not used for scientific purposes. However, the relationship between the EDAC counter and GCR fluxes has been established for a long time and was exploited in [3]. In this study, a procedure was developed using data acquired from *Mars Express* (MEX) and *Rosetta*

(ROS). The same methods were applied here to data from the *Venus Express* (VEX) mission, which was operating from 2005 until 2014. These findings are currently being compiled in a paper for publication in *Planetary and Space Science*.

4.1. Data processing

The data processing procedure is as follows:

1. Correct the zero-resets performed during the mission to keep a monotonically increasing counter.
2. Remove the SEP events corresponding to sudden big increases in the EDAC counter. They are detected by computing the discrete derivative via finite backward difference. Once these rates have been computed, the 99th percentile of their distribution is estimated. The jumps with values above this threshold are thus considered to be due to SEP events and removed from the EDAC curve.
3. Smooth the data by applying a Savitzky-Golay filter with a 365-days window.

This procedure is completed by additional steps to uniformize the data. Figure 11 showcases the result of the data processing on the VEX EDAC.

4.2. GCRs characterization with EDAC slope

The slope of the EDAC counter is computed with a backward finite-difference scheme using a 2-weeks (14 days) window. The expected anti-correlation shape is visible in the two top plots in Figure 12. The bottom plot displays the cross-correlation between the VEX EDAC slope and the Sunspots number representing the solar cycle. The minimum of the curve corresponds to the maximum anti-correlation. As explained in [3], this gives an estimate of the time-lag between galactic cosmic rays and solar cycle. The actual value of this time-lag varies from a few months to 1 year, with some sources even mentioning negative values [1]. Here, the computed time-lag is negligible, with a value of -0.033 months, or 1 day. This could indicate that the influence of the Sun on the GCRs fluxes is near-instantaneous at Venus.

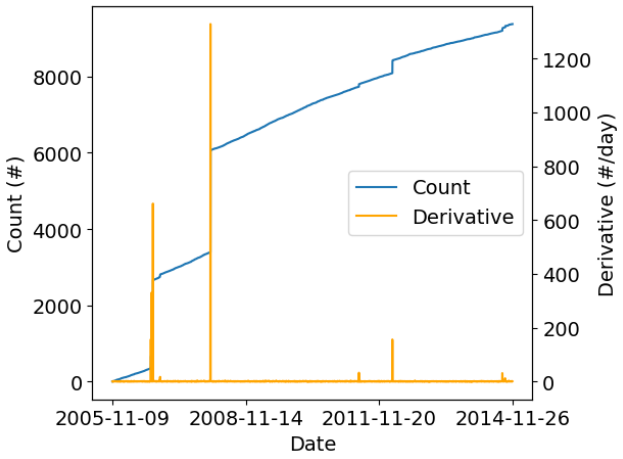

(a) Raw counter and numerical derivative.

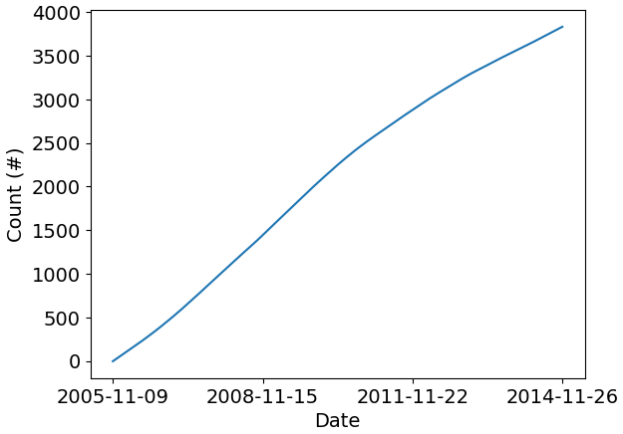

(b) Processed counter (without SEP events and smoothed).

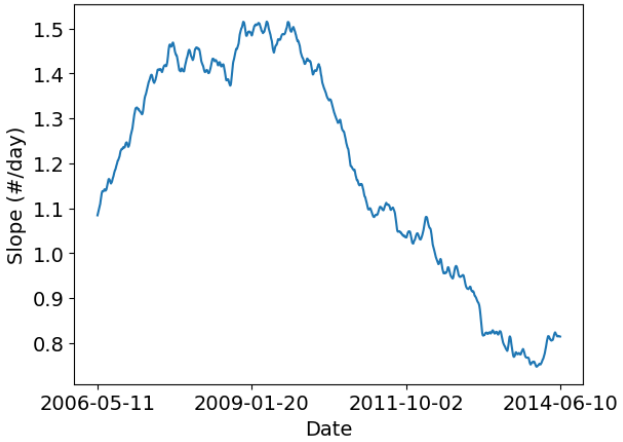

(c) Computed slope.

Figure 11: Data processing on the VEX EDAC counter.

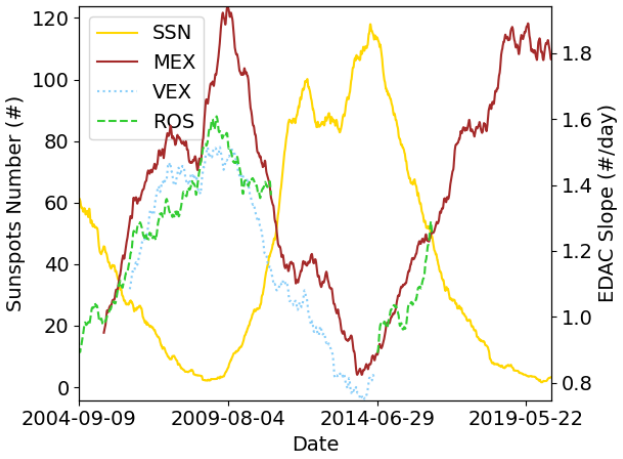

(a) EDAC slope for the three missions (Mars Express, Rosetta, Venus Express) and Sunspots number.

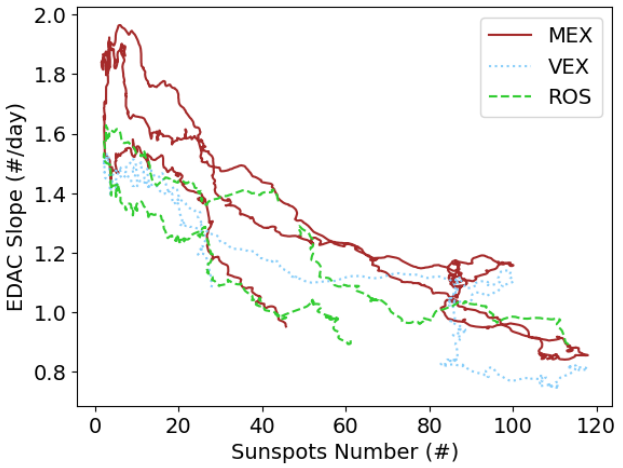

(b) Anti-correlation between the EDAC slopes and the Sunspots number.

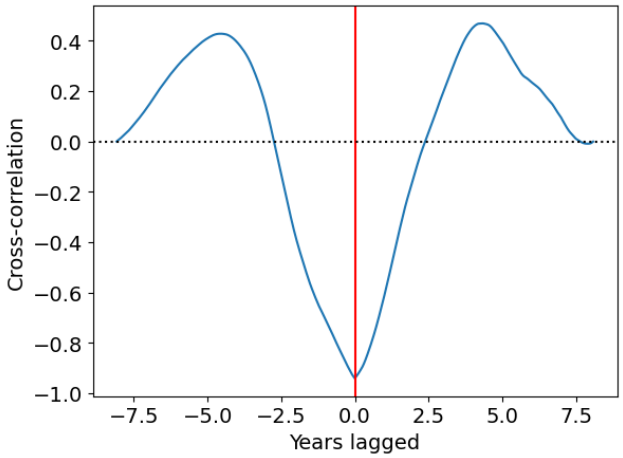

(c) Cross-correlation between the VEX EDAC and the Sunspots number.

Figure 12: Relationship between EDAC slopes and solar cycle.

4.3. Discussion

The procedure described in [3] was expanded on with data from VEX. The results show that the EDAC slope exhibits a very clear anti-correlation with the Sunspots Number (with a correlation coefficient of -0.95 at minimum lag). The VEX curve clearly follows the ones of MEX and ROS previously derived, confirming that the solar modulation exhibits a similar pattern at Venus.

Cross-correlating the EDAC slope with the Sunspots Number results in an almost zero time-lag, which could indicate that the solar activity has a near instantaneous influence on the GCRs fluxes at the orbit of Venus. This differs from the reported value at Earth which, depending on the study, is estimated to be between 2 and 8 months. Comparing the available data shows that VEX records less SEP events than MEX at the same period, indicating that the VEX EDAC is sensitive only to particles in the most energetic part of the GCRs spectrum. This could have an impact on the response of the VEX EDAC to solar modulation and bias the computed lag. These findings need to be further checked with theoretical considerations and models since the distance between the Earth and Venus is relatively small (0.3 AU). [3] investigated the use of ratios between EDAC slopes to disentangle the effects of solar temporal and spatial modulation of GCRs. This was also studied in this thesis but resulted unsuccessful.

As discussed in [3], comparing EDAC data coming from different spacecrafts is not straightforward. The solar modulation of GCRs intensity is rigidity-dependent and particle energies causing SEUs might differ from one spacecraft to another, depending on the location of the onboard computer and the device's shielding. However, the similarities between *Rosetta*, *Mars Express* and *Venus Express* in terms of subsystems and memory devices make us confident that the results coming from this empirical approach hold value. Nonetheless it is important to validate this procedure on future missions carrying both EDAC counters and radiation monitors.

5. Conclusions

This thesis investigated two ways of characterizing GCRs with planetary missions. The first one relied on simulations of particle-detector interactions with a specialized scientific instrument, while the second one involved a more novel analysis of engineering data coming from an instrument dedicated to spacecraft housekeeping. Both allowed to study galactic cosmic rays and their variations in the solar system. The results presented in this thesis should however be validated with further studies. JUICE will arrive to the Jovian system in 2032 and a future mission to Venus might give more insight on the GCRs fluxes closer to the Sun. In the meantime, the considerations described here could be built upon with more advanced simulations. A deeper analysis of the thresholds configuration on RADEM would be useful to set the optimal parameters for the radiation environment at Jupiter, and the novel findings on the time-lag at Venus should be compared with theoretical models to assess their validity within the scientific community.

6. Acknowledgements

T.R. thanks EPFL, PoliMi and ESA-ESTEC for the opportunity and funding to work on this project, as well as USI/SXS-Movetia for the financial support.

References

[1] Badruddin, Singh, M., and Singh, Y. P. *Astronomy and Astrophysics*, 466:697–704, 2007.

[2] Shirvani et al. Software-Implemented EDAC Protection Against SEUs. *IEEE Transactions on Reliability*, 2000.

[3] E.W. Knutsen, O. Witasse, B. Sanchez-Cano, M. Lester, R. F. Wimmer-Schweingruber, M. Denis, J. Godfrey, and A. Johnstone. Galactic cosmic ray modulation at Mars and beyond measured with EDACs on Mars Express and Rosetta. *Astronomy and Astrophysics*, 650:A165, 2021.

[4] A.S. Oates. 7 - Reliability of silicon integrated circuits. In Jonathan Swingler, editor, *Reliability Characterisation of Electrical and Electronic Systems*, pages 115–141. Oxford, 2015.

[5] M. Pinto. *Development of a Directionality Detector and Radiation Hardness Assurance for RADEM, the ESA JUICE mission Radiation Monitor*. PhD thesis, Universidade de Lisboa, 2019.

[6] J.D. Sullivan. Geometric factor and directional response of single and multi-element particle telescopes. *Nuclear Instruments and Methods*, 95:5–11, 1971.